Volume 6 | Number 2 | February 2019 | Pages 201–416

Materials Horizons

rsc.li/materials-horizons

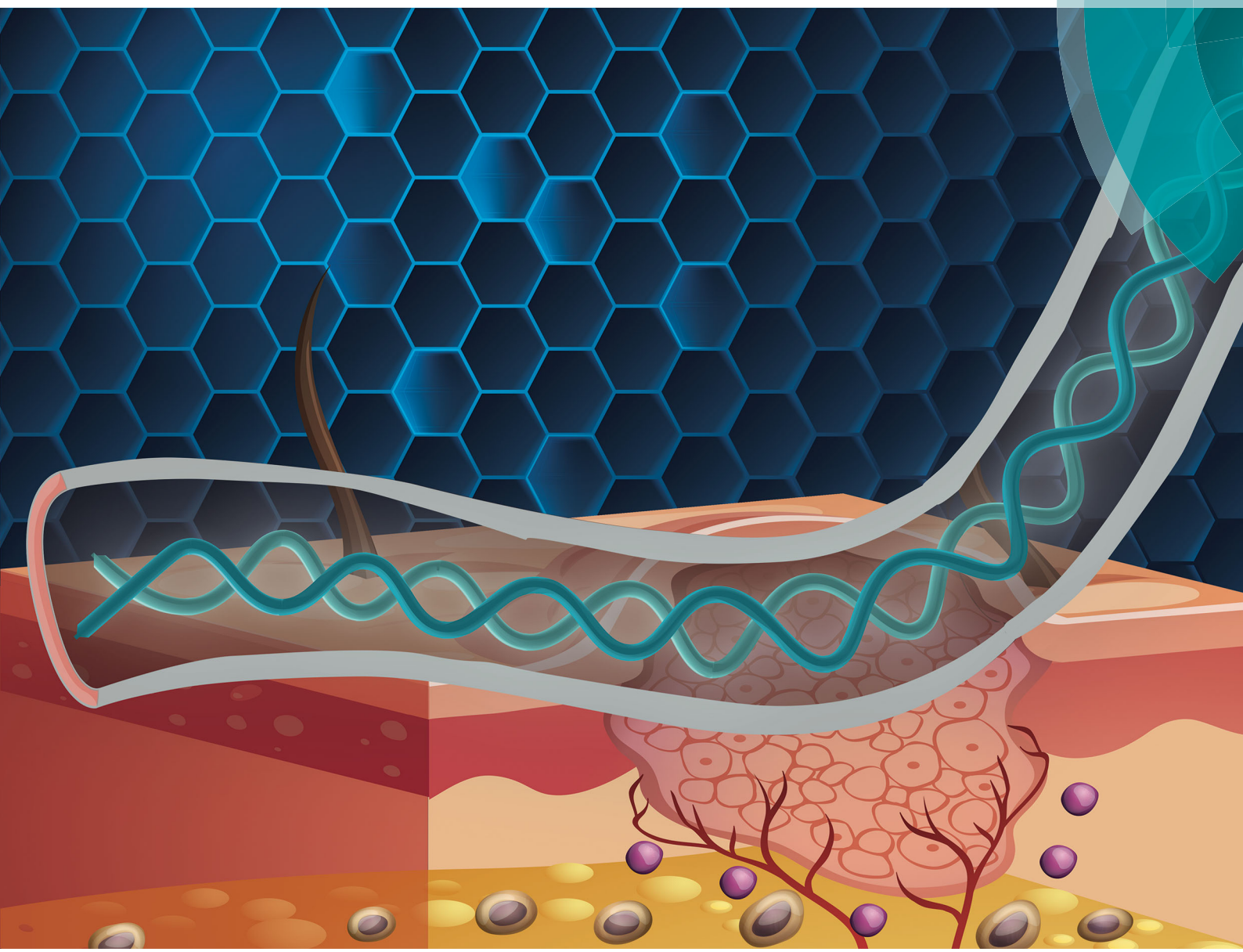

ISSN 2051-6347

ROYAL SOCIETY OF CHEMISTRY | Celebrating IYPT 2019

COMMUNICATION

Monalisa Mukherjee *et al.*

Hydrogel nanotubes with ice helices as exotic nanostructures for diabetic wound healing

Materials Horizons

COMMUNICATION

Cite this: *Mater. Horiz.*, 2019, **6**, 274

Received 15th October 2018,
Accepted 6th December 2018

DOI: 10.1039/c8mh01298a

rsc.li/materials-horizons

Hydrogel nanotubes with ice helices as exotic nanostructures for diabetic wound healing†

Aarti Singh, [a] Rohan Bhattacharya, ‡[ab] Adeeba Shakeel, ‡[b] Arun Kumar Sharma, [c] Sampathkumar Jeevanandham, [d] Ashish Kumar,[c] Sourav Chattopadhyay, [e] Himadri B. Bohidar,[f] Sourabh Ghosh,[g] Sandip Chakrabarti, [d] Satyendra K. Rajput [c] and Monalisa Mukherjee *[ab]

The slings and arrows of two-dimensional (2D) graphene and one-dimensional (1D) carbon nanotubes embody a high risk-to-benefit ratio, which is challenging for their biocompatibility. Herein, we report for the first time the synthesis of hydrogel nanotubes (HNTs) with ice helices as exotic nanostructures *via* free radical-mediated aqueous copolymerization. Extensive embryonic 2D polymer nanosheets were produced after 10 h of reaction which buckled out-of-plane into HNTs, inspired by the ancient art of origami. Water drawn into the hydrophobic hollow conduit freezes spontaneously, acting as an epicenter for the genesis of an ice helix trapped in a kinetically stable arrangement with regular periodicity, extending rational synthesis into the nanoscale regime. In this seminal work, the mechanism for the formation of ice helices inside the HNTs was delineated with the aid of transmission electron microscopy (TEM), X-ray diffraction patterns (XRD) and Raman spectroscopy. Endowed with unique biocompatibility, these HNTs aided the rapid establishment of wound barrier properties with concomitant cell proliferation guided by a provisional matrix mimicking the extracellular matrix niche. The HNTs support a permissive milieu for vascular sufficiency with well-proliferated fibroblasts at the wound bed.

Conceptual insights

With the paradigm shift towards better clinical management of diabetic wounds, safe, effective and economic materials are greatly required. To overcome existing technological hurdles, we report for the first time the fabrication of hydrogel nanotubes (HNTs) with ice helices that address the great limitations of carbon nanotubes in the biomedical arena. 2D polymer nanosheets with hexagonally structured ice locked into the polymer mesh (d = 0.25 nm) was obtained *via* free radical aqueous copolymerisation. In due course of time, the alkyl side chains revealed unique interdigitated packing in a confined geometry and a crystallization pattern armed into a hexagonal rotator phase stabilized by nanoscale confinement. Furthermore, at a particular temperature, these sheets buckled out-of-plane into crystalline hexagonally packed HNTs inspired by the ancient art of origami with a high degree of sophistication, producing a seamless pattern. We envisaged that water inside the hydrophobic channels would freeze spontaneously, clustering in the nano-confined environment and providing a signature for the emergence of a quasi-1D ice helix. These HNTs ameliorated early wound bed restoration *via* reepithelialization and fibroplasia, bolstering angiogenesis in diabetic Wistar rats. A mature epidermal architecture with multiple layers of fibrous connective tissues observed by day 16 indicates complete healing of the wound.

Introduction

The delineation of carbon nanotubes (CNTs) was accentuated by the trailblazing work of Sumio Iijima[1] and continues to extend the limits of imagination. Since their discovery, CNTs have been extensively used in drug delivery,[2] bioimaging,[3] and sensors.[4] However, CNTs potentially pose health and environmental hazards, including carcinogenesis, which inhibits their widespread application.[5,6] Although, different strategies have been adopted for making CNTs biocompatible with the living system,[7,8] it's high surface area[9] unduly jeopardize the health, gaining a level of notoriety in biomedical arena.[10] Baffled at this censorious crossroad, we developed hydrogel nanotubes (HNTs) promising biocompatibility with the living system.

Distinct, functional, tunable nanoscale architectures based on polymeric materials are of great interest because they present tantalizing opportunities for a vast array of applications.[11–13] Hydrogels are three-dimensional, highly hydrophilic, soft polymeric materials that have metamorphosed from basic applications such as contact lenses[14] and scaffolds[15] towards advanced

[a] *Amity Institute of Click Chemistry Research and Studies, Amity University Uttar Pradesh, 201303, Noida, India. E-mail: mmukherjee@amity.edu; Tel: +91-120-4392194, +91-120-503-4586945*
[b] *Amity Institute of Biotechnology, Amity University Uttar Pradesh, 201303, India*
[c] *Amity Institute of Pharmacy, Amity University Uttar Pradesh, 201303, India*
[d] *Amity Institute of Nanotechnology, Amity University Uttar Pradesh, 201303, India*
[e] *Department of Electronics, Ramakrishna Mission Residential College, Narendrapur, Kolkata-700103, India*
[f] *School of Physical Sciences, Jawaharlal Nehru University, New Mehrauli Road, New Delhi, Delhi 110067, India*
[g] *Department of Textile Technology, Indian Institute of Technology Delhi, New Delhi, 110016, India*

† Electronic supplementary information (ESI) available: Fig. S1–S9, Tables S1 and S2. See DOI: 10.1039/c8mh01298a

‡ These authors contributed equally as the second author.

biomaterials which can be attuned to mimic specific niches for tissue regeneration[16,17] and can be utilized *in vitro* and *in vivo* as drug delivery platforms.[18,19] Hydrogels can function as wound healing agents because they are capable of retaining water vapor at the site of the wound, impeding penetration of various proteins[20,21] and thereby preventing wound desiccation. Synthetic hydrogels offer the additional benefits of facile processing, high purity, lack of intrinsic activity and good mechanical strength due to their distinguished intelligence, unlike natural polymers, which exhibit batch-to-batch variations.[22]

Various synthetic procedures, such as template membranes,[23] chemical vapor deposition,[24] layer-by-layer assemblies,[25] and wetting approaches,[26] have been utilized for the fabrication of polymer nanotubes. However, the development of well-controlled and flexible architectures in the nanoscale regime is a typical stumbling block hindering the formation of long nanotubes. Aqueous co-polymerization is a promising method to minimise this gap.[27] Additionally, fluid phase transition within nano-confinement has been mostly limited to intricate theoretical interpretation *via* molecular dynamics (MD) simulation studies.[28–33] At present, there is great emphasis on the rapid development of materials with well-controlled architectures.[34] Structures containing complex morphologies, such as tubules, helices, multi-compartments, and multicores, account for exotic nanostructures with biomedical suitability.[35] In particular, the quest to unlock the morphologies of exotic nanostructures requires multidimensional understanding with a high degree of molecular customization to add biomimetic features to synthetic polymers for next-generation applications.

For commercial purposes, synthetic polymers are mostly developed using free radical polymerization of vinyl monomers.[36,37] However, their limitation lies in poor control over the mechanism, which perturbs the growth of well-defined and controlled chain architectures.[37] In this communication, to overcome this limitation, we report a facile, cost-effective, template-free, controlled radical polymerization that is adapted to leverage therapeutically promising outcomes *via* material design through an aqueous copolymerization reaction at 40 °C with acrylic acid (AAc) and *N*-[3-(dimethylamino)propyl]methacrylamide (DMAPMA) without any coating. Impressively, the sample collected after 10 h of continuous reaction revealed two-dimensional (2D) sheets. In due course of time, nucleated folds propagated along the surface, facilitating sheet enclosure in an origami-like fashion to form well-defined tubular structures. Water locked within the polymeric mesh formed hexagonally structured ice with a mainly AB Bernal stacking pattern as revealed by high-resolution transmission electron microscopy (HRTEM). Water drawn into the hollow internal conduit froze due to nano-confinement, forming an ice helix with almost regular periodicity (Fig. 1). This is the first report describing the presence of ice helices within HNTs. To elucidate the role of temperature in the formation of the HNTs, we investigated the polymerization process at different temperatures. Plausibly high enthalpy perturbed the sheets from rolling into a tube which comprises mainly of bulk water as evident from our HRTEM, X-ray Diffraction (XRD) and Raman spectroscopic studies.

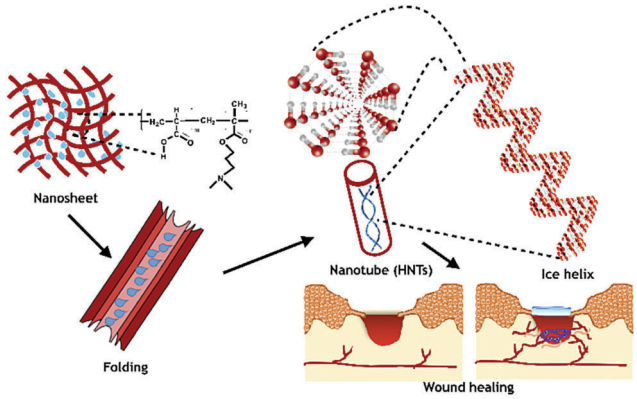

Fig. 1 Schematic of the formation of hydrogel nanotubes (HNTs) *via* self-rolling of polymer nanosheets at 40 °C with ice helices entrapped in their hollow channels and their application in diabetic wound healing.

The HNTs depicted nano-to-micro hierarchical patterns, as observed in the soft membranes surrounding living cells, imparting them with properties that can be varied in response to performance. Endowed with tunable physical properties, the HNTs can slowly release their therapeutic payloads at a particular pH in a controlled fashion, improving their pharmacokinetics. The HNTs also exhibited appreciable mechanical strength and good viscoelastic properties. The HNTs favored accelerated angiogenesis, ensuring proper blood perfusion, collagen deposition and keratinocyte migration in the wound bed and resulting in complete wound closure by day 16 in diabetic Wistar rats. These ampholytes may interact non-covalently with the wound bed, forming macromolecular complexes with proteins through hydrogen bonding and potentially mopping up pro-inflammatory cytokines, thus generating functional microvasculature. Uniting the features of both nano- and microscale domains provides better properties to HNTs for their enhanced performance and increased efficacy. Bequeathed with superior biocompatibility, these HNTs are fortified to be a versatile toolbox that ensures facile application and repositioning and accommodates dynamic movement of tissue at the site, addressing the incessant concern of the dysfunctional healing process of diabetic wounds and maintaining a constantly moist environment without any growth factor supplementation.

Results and discussion

The change in interfacial tension between water and the electrolytic complex of DMAPMA and AAc causes the polymeric chains to associate, engendering precipitation of the polymer complex (Fig. 2a and b). The congregation of these precipitates is guided by facial amphiphilicity, where the solvation free energy of these assemblies becomes lower than that of the individual solvated assemblies, thereby forming a gateway for aggregate formation. The preferential solvation of PAAc in water within the PADP complex limits the interfacial curvature between hydrophilic corona and hydrophobic core proving it to be the biggest player in the game of HNT formation.

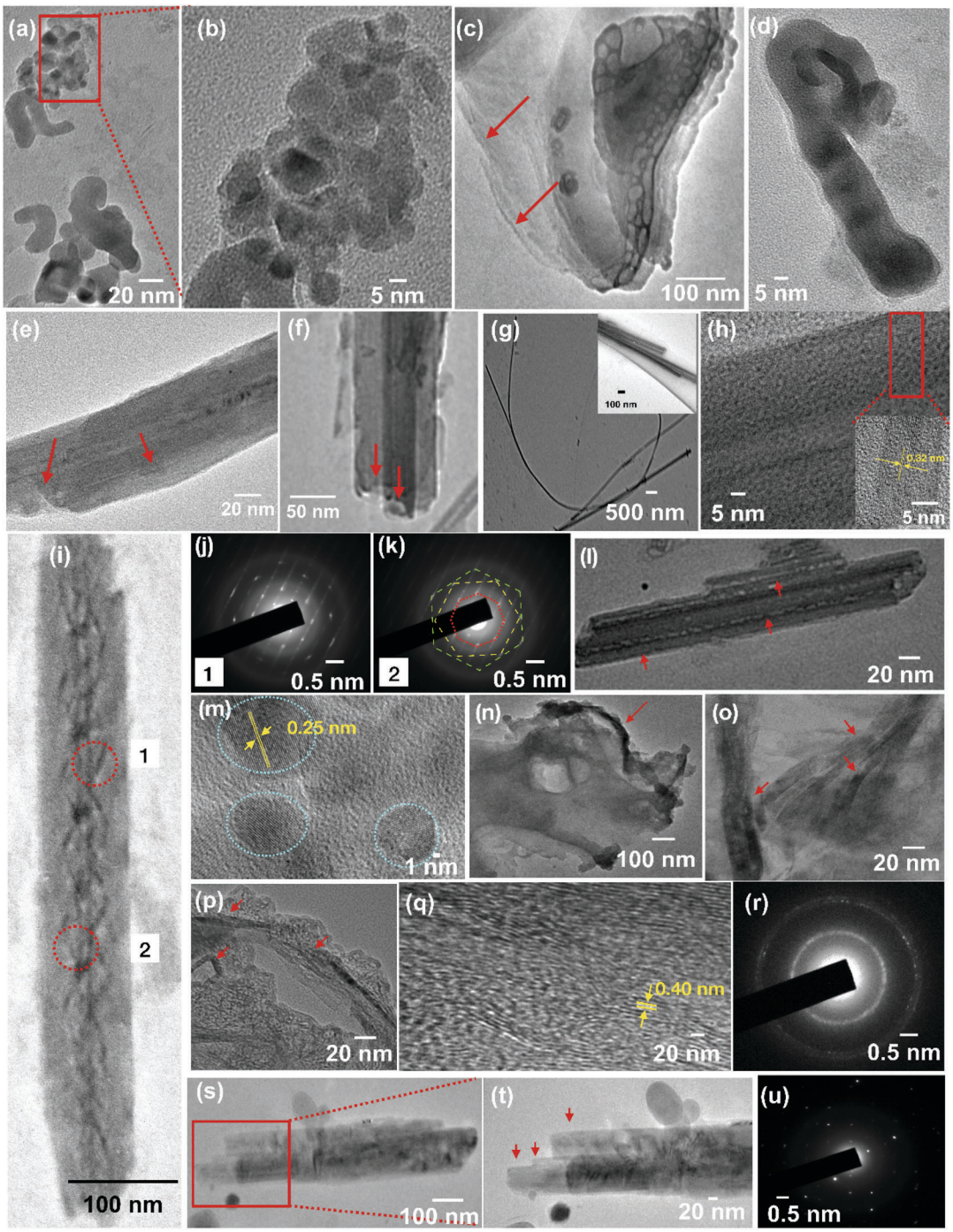

Fig. 2 Morphological characterization of PADPs. (a and b) TEM micrographs of the polymeric complex. (c) HRTEM image showing stacked polymer nanosheets after 10 h (arrows indicate embryonic polymer nanosheets with lateral dimensions in the nanometer range). (d) 'Pitcher'-like architecture. (e and f) A tubular structure formed from rolling up of polymer nanosheets in PADP 40 to form HNTs (arrows indicate warping of the sheets). (g) Flexible HNTs at low magnification. (h) HRTEM image of the HNTs. (i) HNTs with ice helices. (j and k) SAED patterns corresponding to areas (1) and (2) in the image (i). (l) Bundle of HNTs (arrows indicate ice helices entrapped within the HNTs). (m) Hexagonally structured ice. (n–r) TEM micrographs of PADP 60: (n and o) Crumpled polymer nanosheets. (p) Distorted tubular architecture. (q) Disordered alkyl stacking in polymer nanosheets. (r) SAED pattern. (s–u) TEM micrographs of PADP 80: (s and t) Distorted tubular architecture. (u) SAED pattern.

The flexible polymer side chains displayed unique interdigitated packing, maximizing their van der Waals contacts and crystallization patterns, whereas the volume of the main chain was too large to take part in crystallization. The distribution density and grafting degree of the alkyl side chains with regular conformations along the polymer main chains gave rise to a hierarchical self-assembly, forming extended two-dimensional (2D) islands. Extensive growth of embryonic polymeric layers

(Fig. 2c) was observed in the aliquots taken after 10 h of continuous reaction; they assembled to form pitcher-like architectures. (Fig. 2d) Furthermore, nanoscopic confinement-mediated crystallization behavior of the frustrated side chains was guided by the rigidity of the polymer main chain, affording different thermodynamic and crystallization behaviors in metastable crystalline phase. As the flexible side chains attained a critical length, they exhibited thermotropic phase transition behavior, packing into hexagonal rotator phases stabilised in a nano-confined environment; thus, they exhibit unique diffraction XRD patterns for the HNTs. The main chain primarily constituted the disordered phase, whereas the side chain crystallites in the polymer backbone exhibited a layered long range hexagonal crystal architecture.[38] Furthermore, the poorly translucent nature of our HNTs manifests low vitrification of the amorphous main chains and high crystallinity of the side chains.

In due course of polymerization, these polymer nanosheets are subjected to stacking and roll up in a preferential direction (Fig. 2e), stabilizing the orientation order at 40 °C and subsequently zipping the polymer nanosheets into tubes. This curvature-induced strain exerts a transverse gradient of stress that concentrically rolls the stacked sheets, guided by van der Waals interactions, with a hollow internal cylindrical conduit (Fig. 2f); this offers a unique avenue for nanoconfinement governed by polymer chain dynamics. Water nanodroplets can also countermand the deformation barrier, inducing rapid rolling of the planar nanostructures at a particular temperature.[39] The low viscosity of water favors damage-free assembly *via* frictionless feeding, forming high-quality HNTs. Possibly, a low ratio between the hydrophilic corona and hydrophobic core governs the 'bent' nature of HNTs compared to the straight tubes. The length variability of the tubes further validates this hypothesis (Fig. 2g).

Using HRTEM, we performed a systematic exploration of the folding of the polymer nanosheets. The in-plane lattice spacing of 0.32 nm is close to that of graphene due to the low energy gain by local stacking (Fig. 2h). We noted that after 24 h, the nanotubes were super-aligned, arising from the alignment of the tubes dominated by the van der Waals interactions (Fig. 2h). We set out to investigate the hollow tubular structures; the bright patterned central area and dark walls demonstrated the important hallmarks of a 'capillary-like' architecture, opening a new vista for nanofluidics (Fig. 2h). The outer diameter is $\sim$61 nm, whereas the inner diameter is $\sim$3 nm (Fig. S1, ESI†). Some of the tubes were observed to bunch and remained distinct throughout, revealing their flexible characteristics (Fig. 2f and g).

Water locked within the polymer meshes formed hexagonal ice, exhibiting both AA and AB Bernal stacking patterns; the AA patterns succumbed to extensive defect states upon electron bombardment due to erratic hydrogen bonding. However, inter-stratified hydrogen bonding between the hydrogen atom in one layer and the oxygen atom in the opposite layer is accountable for the relative abundance of the AB Bernal stacking pattern with a long-range crystalline order[33] (Fig. 2m). The in-plane lattice spacing of 0.25 nm matches well with the distance of the oxygen columns in the observed direction.[40,41]

A startling feature was observed in PADP 40, where the entrapped water molecules of the inner tube formed a hydrogen-bonded network exhibiting a dramatic dimensionally-confined phase transition to cyclic puckered eight-membered ring conformations, satisfying the 'bulk ice' rule[31,42] (Fig. 2l). The adherence of water at higher concentrations to the inner coronal wall reduces the energy barrier along the tube axis, facilitating migration of water into the interior of the tube.[29] The enthalpy cost in this environment and extensive non-covalent interactions may enable this phase transition.[42]

The anisotropic growth mode *via* nucleated self-assembly accompanied by staggered stacking of nano-crystalline water led to a dramatic contraction of the corona volume due to a uniaxial compressive force parallel to the HNT axis, giving rise to a high degree of cooperativity. Confinement-induced entropy-aggravated buckling of the ice inside the nanotubes fostered distortion and reformation of the hydrogen bond framework, thereby causing the ice to curl into a kinetically stable helix (Fig. 2i). Interestingly, this ice helix resembles a DNA molecule or helical contortions of vines entangled around a tube.

The foundation of the kinetically stable arrangement of the ice helix is undoubtedly a testament to the versatility and unique geometric distribution of the water and hydrogen bond framework, where most of the water molecules are involved in hydrogen bonding with the previous non-dangling hydrogen and succeeding oxygen of water molecules, leaving one hydrogen atom free. This hydrogen-bonded network alters the reorientation dynamics of the confined ice, which manifests in energetically significant interactions with the hydrophobic cores of the HNTs while others ally with the nanotube axis, serving as a mimic of biological ion channels. We envisage that the ice helix is mainly composed of octagonal rings with few defects at the peripheries, where the helix twists and turns to maintain its helicity[31] (Fig. 2j and k).

The SAED pattern resembles multi-walled nanotubes. The bright spots are aligned perpendicular to the tube axis produced by the diffraction of the parallel quasi-planes in Fig. 2(i–k). The set of split spots arises because the tubes are nearly perpendicular, with a chiral angle of 20.99° (Fig. S2, ESI†). The intensity of the spots increases in the direction of the tube axis, elongates away from the tube axis and finishes at the nominal hexagonal positions (Fig. 2j and k). The indexed (h k 0) planes emerge from the core of the HNTs, which further relates to the curvature and alignment of the nanotubes in the direction normal to the tube axis[43] (Fig. S2, ESI†). We propose that the crystallinity kinetics is bolstered by confinement-induced effects that restrict the chain mobility at the free surface.[44] The presence of high-order reflections suggests that the packing has a long-range order perpendicular to the tube axis. To the best of our knowledge, this is the first report of a cage-shaped octagonal geometry, as visualized in the inner circle of the SAED pattern of the HNTs (Fig. 2j and k) pertaining to the ice helix.[45]

During copolymerization at 60 °C, several distorted polymer nanosheets were observed; however, from an enthalpic standpoint, these sheets could not be rolled into tubes (Fig. 2n and o). However, we could observe rolling of the nanosheets in one place, but it was highly distorted (Fig. 2p). The irregular crystallinity in certain domains arises from water islands trapped between the polymer nano-sheets, incurring electrostatic repulsion of the pendant groups and segregated arrangements of the alkyl nanodomains (Fig. 2q). This result was further validated by the diffused ring patterns with faint spots in the SAED (*d*-spacing = 0.40 nm) (Fig. 2r).

At 80 °C, however, thermal expansion of two adherent layers causes differential stress relaxation driven by water flux, guiding plastic deformation of the polymer matrix of PADP 80 (Fig. 2s and t). In due course of time, water evaporates from the crevices, facilitating interaction of the alkyl side chains and leading to irregular crystallinity. The bright sets of spots in the SAED pattern can be indexed to polycrystallinity of the polymeric side chains (Fig. 2t).

XRD provides dynamic information about the architecture of HNTs at a spatiotemporal resolution. The broad and weak reflection pattern at $\sim 9^\circ$ 2θ of the HNTs is attributed to the unique packing[46] of the methylene backbones within the alkyl nanodomains,[47] which expels the bulk water from the conduit due to van der Waals forces; this demonstrates an ordered orientation and translation to HNTs underpinned by the (001) reflection (Fig. S3a, ESI†). The decreased peak intensity at $\sim 9^\circ$ 2θ for the HNTs indicates the adsorption of water, which is converted to an ice helix in the nanoconfined environment (Fig. S3a, ESI†). In PADP 60, bulk water did not escape from the interstitial sites of the polymer nanosheets but instead caused protonation and deprotonation of the pendant groups within the polymer chains; this resulted in electrostatic repulsion and segregated arrangements of the alkyl nanodomains, inhibiting the unique packing and preventing nanotube formation (Fig. S3b, ESI†). At 80 °C, the bulk water greatly evaporated, creating space for van der Waals interactions between the alkyl side chains, which may result in nanotubular structures; however, the high entropy of the polymer chains at this temperature resulted in a 'flat noodle'-like morphology.

Curvature-induced strain and the stacking order of the polymer nanosheets introduced a characteristic broad peak centred at $\sim 20^\circ$ 2θ; this was assigned to the (100) plane, corresponding to alkyl stacking for the HNTs, PADP 60 and PADP 80[48] (Fig. S3a–c, ESI†). Bulk water trapped in the interstitial sites of the polymer nanosheets perturbed the unique arrangement of alkyl nanodomains into the hexagonal rotator phase in PADP 60; this is more effective in diffracting X-rays, with an intense reflection at $\sim 20^\circ$ 2θ (*d* spacing = 0.42 nm) (Fig. S3b, ESI†). Interestingly, as water molecules were adsorbed at the conduit of the HNTs, subtractive superposition of the X-rays from the alkyl nanodomains and water resulted in suppression and broadening of the peak, which reinforces the presence of ice inside the nanotubes (Fig. S3a, ESI†). Plausibly, the co-existence of 2 peaks in the slow scan of the HNTs (PADP 40) at $\sim 9^\circ$ 2θ and $\sim 20^\circ$ 2θ indicates the presence of two long-range ordered 1D ice helices, which matches Fig. 2i.[49]

The appearance of a new peak at $\sim 26^\circ$ 2θ and the simultaneous decrease of the peak at $\sim 20^\circ$ 2θ for the HNTs arises due to nanoconfinement-mediated unique packing of the alkyl side chains of the polymer mesh into the hexagonal rotator phase along the (002) plane (Fig. S3a inset, ESI†). This peak is also associated with the hexagonal-structured ice entrapped within the polymer meshes. We believe that the excellent alignment of the HNTs, sheet multiplicity, interlayer distances, diameter dispersivity, and orientation of the tubes are the major causes of the monotonic decrease of the peak intensity.[50] The well-ordered structure is reinforced by the narrow FWHM. We could not observe any diffraction peaks in this region for PADP 60 or 80, indicating the absence of interdigitated packing due to the enthalpic penalty at a higher temperature.

Fig. 3a accentuates the interconnected honeycomb structure of the HNTs after swelling in PBS buffer (pH 7.4). We envisage that the anisotropic growth mode is instrumental in obtaining the high cell to wall ratio with uniformly distributed pores, confirming the structural efficiency. Furthermore, this macroporous structure is attributed to the presence of acidic (carboxylic) and basic (amide) functional groups that undergo protonation and deprotonation in response to pH, which leads to the formation of internal crosslinked networks. Fig. 3b shows interconnected nano-globules, which are believed to impart strength because they remain intact at high swelling, preventing the gels from disintegrating. Furthermore, the outer wall was seen to be continuous and free of pores or cracks (Fig. 3c).

Upon deswelling, the delaminated regions of the polymer sheets are subjected to warping under uniaxial forces, developing parallel ridges on the surface and giving rise to a stripped architecture (Fig. 3d). Depending on the composition of the copolymer, the interfacial energy drives contortion of delaminated buckles along the ridge, thereby partially collapsing the structure. A fresh buckle develops perpendicular to the existing one, giving rise to a labyrinth-like architecture, as shown in Fig. 3e. The wrinkles formed at the sites of orthogonal warping give rise to characteristic corrugation resembling crumpled graphene (Fig. 3f). Simultaneous warping and relaxation of the sheets gives rise to a fascinating pattern of ridges and vertices, which may be due to thermal vibration of the 2D lattice and edge instability (Fig. 3f). These wrinkles ultimately transform into folds under uniaxial forces.

The tubular morphology as portrayed in the SEM images of the HNTs resembles stilt-roots (Fig. 3g). Low HNT density and minimal interaction with the surrounding environment favored mostly solitary growth of sparsely aligned nanotubes, highlighting the ability of the HNTs to stand independently (Fig. 3h). The HNTs exhibited more or less continuous outer walls without any kink-bands or cracking on both the torsion and compression sides.

In Fig. 3i, an incompletely wrapped tube was observed. It seems that one end of the wrinkled sheet was rigidly attached to the HNTs which got rolled up along the tube and stay connected transversely by a commissural fold. A braided structure can be observed in Fig. 3j, which demonstrates the

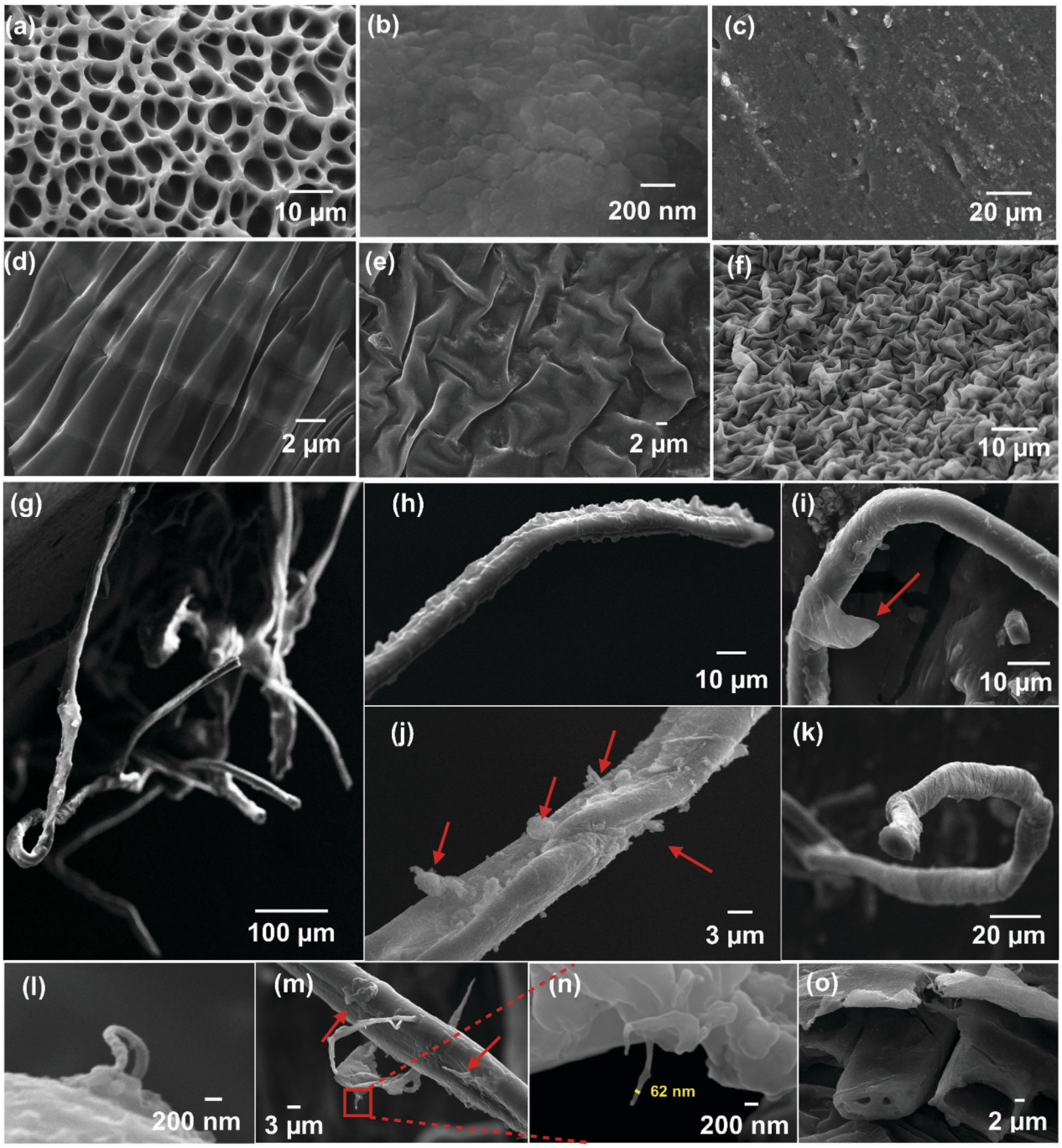

Fig. 3 Scanning electron micrographs of the HNTs. (a) Honeycomb structure after swelling. (b) Nanoglobular architecture. (c) Outer wall. (d) Stripped architecture of polymer nanosheets after de-swelling. (e) Labyrinth-like architecture. (f) Polymer wrinkles. (g) Cluster of HNTs. (h) Alignment of HNTs. (i) A polymer nanosheet transversely connected to an HNT (arrow indicates a commissural fold). (j) Braided architecture (arrows indicate several nucleating daughter folds). (k) Flexible HNTs. (l) Unfurled knot. (m) Hairpin turns arising from a parent tube (arrows indicate several nucleating folds). (n) HNT with a diameter of ~62 nm. (o) Hollow tubular structure.

structural irregularity of a few HNTs arising from stress asymmetry. From a structural standpoint, the tubes exhibited almost uniform diameters with well-designed patterns. The nanotubes survived extreme radii of curvature in the folded and twisted regions, confirming their high flexibility (Fig. 3h–l). This flexibility of the tubes was observed at both the micro and nano scale (Fig. 3l), reflecting that the nano-to-micro hierarchical pattern of the assembly formed well-resolved HNTs (Fig. 3m and n).

In some regions of the tubes, we observed branching points (Fig. 3j and m) where rectangular sheets were firmly attached to the nodes (Fig. 3m). This sheet was subjected to Fermat-type twisting from which a new morphological phase emerged, giving rise to hairpin turns (Fig. 3m). We observed these hairpin

turns at a number of locations, where nucleating folds further subdivided into daughter folds over multiple generations and stagnated. In some cases, the folds presented a knotted architecture which unfurled upon electron bombardment (Fig. 3l).

A hollow tubular structure can be observed in Fig. 3o for the HNTs draped with sheets. In contrast, distorted tubular structures were observed for PADP 60 (Fig. S4a–c, ESI†), whereas in PADP 80, an isolated ribbon-like morphology was noted, where insufficient twists generated an inhomogeneous surface morphology (Fig. S4d–f, ESI†).

Raman spectroscopy was used to validate the chemical fingerprints of the HNTs; the first spectral signature appears at $\sim$486 cm^{-1} due to the breathing modes of the small-diameter inner tubes of the rolled-up polymer nanosheets for symmetric in-phase radial displacements of all the carbon atoms lining the HNTs (Fig. 4). This peak indicates the low structural deformation of the tubes. The sharp, low-intensity peak at $\sim$878 cm^{-1} was ascribed to rotational excitation along with the lattice phonons of hydrogen-bonded water, inferring well-ordered H atoms on discrete lattice planes.[52] The peak centered at $\sim$933 cm^{-1} provides insight into the stereoregularity of polymers that orient themselves *via* distinct assembly of side chains, leading to a metastable crystalline morphology.

The characteristic peak at $\sim$1290 cm^{-1} originates from the alkyl side chains in the crystalline domains,[53] whereas the peak at $\sim$1329 cm^{-1} accounts for –CH_2– wagging for PADP 60. This peak is obliterated by the ice helix in the HNTs (PADP 40), which shields the –CH_2– groups in the interior of the tube. Characteristic conjugate peaks at $\sim$1418 cm^{-1}, $\sim$1453 cm^{-1}, $\sim$1414 cm^{-1}, and $\sim$1466 cm^{-1} are associated with symmetric and asymmetric bending of the terminal CH_3 groups for PADP 60 and PADP 80, respectively. However, for the HNTs, these vibrations are red-shifted towards $\sim$1415 cm^{-1} and $\sim$1443 cm^{-1}, respectively, due to associative interactions with water molecules (Fig. 4).

Additionally, the peak at $\sim$1346 cm^{-1} relates to the wagging of CH_3 groups in the HNTs and PADP 60 and 80. The peak at $\sim$1711 cm^{-1} enumerates the stretching vibrations of C=O. In the HNTs, the water molecules become kinetically trapped in the polymer matrix due to the physical constraints introduced by the heavy meshes, leading to a peak for hexagonal-structured ice at $\sim$1770 cm^{-1}. This result is in good agreement with the 26° 2θ (002) peak of the HNTs in the XRD spectra. Similar results were recently reported by Zhu *et al.*[33] The charge and van der Waals potential of carbonyl oxygen are substantially greater than those of hydroxyl oxygen; therefore, carbonyl oxygen preferentially forms hydrogen bonds with water molecules.

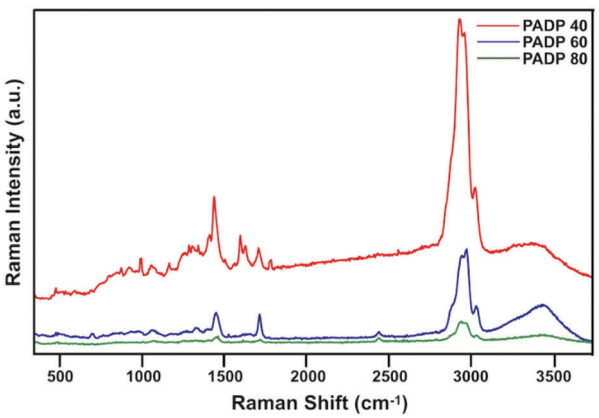

Fig. 4 RAMAN spectra of PADP 40 (HNTs), PADP 60, and PADP 80.

The blue-shifted peaks centered at $\sim$1719 cm^{-1} and $\sim$1723 cm^{-1} for PADP 60 and 80, respectively, indicate the presence of free C=O moieties. The distinct peaks at $\sim$1602 cm^{-1} and $\sim$1633 cm^{-1} arise due to symmetric and antisymmetric O–H bending vibrations of the HNTs, providing an accurate benchmark for ice spiraling along the HNT axis which is absent in the spectra of PADP 60 and 80. The co-existence of sharp and intense peaks at $\sim$2933 cm^{-1} and $\sim$2962 cm^{-1} indicates symmetric and asymmetric stretching vibrations of –CH_2– groups. The higher intensity of these peaks for the HNTs compared to PADP 60 and 80 depicts maximum polarisation of the alkyl nanodomains. Moreover, water located at the interstitial sites in PADP 60 and 80 substantially masks the stretching vibrations of –CH_2– with a concomitant increase in the O–H stretching vibrations, reflecting the presence of bulk water. The peaks centered at $\sim$3031 cm^{-1} and $\sim$3038 cm^{-1} are attributed to the N–H (secondary amine) stretching mode; these peaks are red shifted for the HNTs due to the strain imposed by the lone pair of electrons and hydrogen bonding with water in the inner coronal wall of the HNTs.

Furthermore, the dense mesh of the HNTs weakens the diffusion of water across the polymer matrix, increasing the density of hydrogen bonds between the polymer and trapped water molecules and imprisoning new water molecules in the meshes. As a result, hexagonally structured ice gives a broad hump at $\sim$3347 cm^{-1} for the HNTs which is intensified for PADP 60; this peak indicates the presence of bulk water and is almost absent in the spectrum of PADP 80. This vibrational permutation underscores the presence of nano-crystalline water in the HNTs. The hump at $\sim$3375 cm^{-1} unequivocally relates to the bulk water in PADP 60. We could not observe any peak in this region for PADP 80 because most of the water molecules evaporated during the polymerization reaction (Fig. 4).

Confinement-induced splitting of O–H vibrations was observed in the FTIR spectra (Fig. S5, ESI†). The antisymmetric and symmetric bending vibrations of O–H can be observed at $\sim$1602 cm^{-1} and $\sim$1646 cm^{-1}, respectively, whereas the peaks at $\sim$3543 cm^{-1} and $\sim$3446 cm^{-1} correspond to double-donor antisymmetric and symmetric O–H stretching vibrations; these peaks are not observed in the spectra of PADP 60 and 80. The dangling O–H groups are reduced in the HNTs, which can be corroborated by the weak broad hump at $\sim$3698 cm^{-1}. In contrast, for PADP 60 and 80, the O–H stretching vibrations are blue shifted to $\sim$3741 cm^{-1}, indicating the presence of free O–H groups at the surface. The sharp peak at $\sim$3407 cm^{-1} originates from the O–H stretching mode of the octagonal ice helices inside the HNTs;[51] this peak is absent in the spectra of PADP 60 and 80. The peaks at $\sim$2345 cm^{-1} in the spectra of the HNTs, PADP 60 and PADP 80 signify sp^3 C–H stretching

vibrations. This peak is weakened in the spectrum of the HNTs; this indicates the presence of ice in the tubes, which conceals the C–H vibrations.

The transition of water in polymer–water systems emerging due to electrostatic hydration effects of amphoteric polymers can be thermally scrutinized by TGA and calorimetric analyses. DSC analysis predicts the sublimated, molten and vaporized stages of sorbed water within the HNTs. Fig. S6a, ESI† shows the DSC thermograms of the HNTs, indicating the temperature range of the glass transition state (ΔT_g), which starts at 114.06 °C and extends to 131.44 °C. This copolymer procures a single glass transition (T_g) at 123.02 °C, indicating a homogeneous nature with some regular physical dispersion; this is similar to previous studies.[54] As can be seen from the thermogram studies, the T_g value of the HNTs lies between the those of the two individual homopolymers, which is characteristic of miscible homogeneous copolymers.[55]

The positive endotherm presents a broad range of enthalpies of fusion (ΔH_f), absorbing 72.648 J g^{-1} of energy in the transition state with an apparent mass loss at ~100 °C; this can be attributed to the loss of structured water entrapped in the polymer matrix. The restraining effect of the charged ions at the polymeric backbone decreases the chain mobility, emphasizing the proximity of crystalline structures over the amorphous domains.[56,57]

The TGA thermogram of the HNTs shows that they undergo three-step thermal degradation (Fig. S6b, ESI†). The first degradation starts at ~80 °C and ranges to ~173 °C with a mass loss of 7% to 18%; this is attributed to water adsorbed in the intrinsic linkages of the polymer. The second thermal breakdown step starts at 242 °C and increases to 330 °C; this may be due to degeneration of the flanking moieties in the polymer chains, where the HNTs lose ~40% of their total weight. The final step of degradation at ~450 °C was accompanied by 95% weight loss due to the breakdown of the polymer backbone.

The mechanical strength, viscoelastic properties, and flexibility of polymers are key factors that determine their performance in wound healing and other biomedical applications. In order to withstand shear, tension and compression forces without failure, the stiffness and flexibility of the HNTs should mimic the normal tissue environment.

The mechanical profile of the HNTs showed the formation of a polyampholyte densely crosslinked network of AAc and DMAPMA copolymers, naturally providing robust mechanical properties at ambient atmospheric conditions. The covalent cross-linking of these amphiphilic copolymers even in the absence of conventional coupling agents enables their applications in soft tissue engineering and wound healing.

Forces of two different magnitudes (9.14 N and 8.44 N) were applied on the HNTs, inducing intramural compressive stress on the HNT network (Fig. S6c and d, ESI†). The backbone of our crosslinked polymer shows a high compressive modulus, which may be instrumental in molding its properties for a wide range of applications. The maximum compressive strength extended to 34 kPa (Table S2, ESI†), exhibiting remarkable competency compared to other conventional polyacrylamide (PAAm) hydrogels.[58,59] The physically crosslinked framework of these hydrogels provides fair mechanical strength due to their well-connected pores, which enable even distribution of the load. The large pore size provides a room for large deformation before failure, imparting good flexibility; thus, these gels are highly suitable for wound treatment. The higher degree of tolerability in terms of deformation extended from compressibility of 27% from the initial point, reaching an ultimate endurance of 89% before terminating at the fracture point or failure (Table S2, ESI†). When the HNTs are constrained externally, the intramolecular crosslinked matrix perpetuates the elasticity during deformation and controls the swelling of the gel. Moreover, the assimilated retracting force on these polymeric networks is transmuted into dissociated and dissipated energy, which enables the networks to reassemble upon unloading in the phenomenon of self-recovery.[58]

The HNTs showed variations in equilibrium swelling depending on chemical cues such as pH, behaving as typical ampholytes with an isoelectric point (pI) of ~3.5. (Fig. S7a, ESI†) It has already been established that amphiphilic physically cross-linked hydrogels imbibe solvent depending on the pH and ionic concentration of the solvent. When submerged in a suitable solvent, the chains in the network become solvated. At pH < pI, the DMAPMA units [$-N(CH_3)_2H^+$] become protonated, causing electrostatic repulsion and resulting in swelling of the HNTs, whereas at pH > pI, deprotonation of the AAc units (–COO–) is responsible for swelling at higher pH. The HNTs attained a maximum swelling of ~2000% at pH 7.4 in 24 h.[60]

The rate of swelling and *in vitro* release involve an interesting interplay of forces restricting network deformation and osmosis that leads to water absorption. Our HNTs loaded with benzalkonium chloride (BZC) exhibited a two-stage drug release profile (Fig. S7b, ESI†). At neutral pH (~7.4), the carboxylic acid moieties are deprotonated, which favors osmosis and causes faster release at the initial period. However, we also observed a decreased release rate with time. The obtained release profile implies that BZC is not only loaded on the surface of the nanotubes but is also taken up within the internal conduit of the HNTs, resulting in sustained release. The low pore surface-to-internal volume ratio and the ice helix in the hydrophobic confinement induce a significant frictional drag that decelerates drug transport, thereby aiding extended release, as more than 88% of BZC was released within 20 h.

Rheological experiments were performed to analyze the mechanical strength of the synthesized HNTs; they were subjected to isothermal frequency sweep experiments to probe their mechanical dispersion. Fig. S7c, ESI† shows that G' and G'' remained unchanged with increasing frequency. Moreover, G' was appreciably higher than G'', indicating that the HNTs were stable in the swollen state, whereas the samples were found to be associated with smaller storage modulus values, denoting their soft nature.

To summarise the aforesaid results, higher values of G' (6.235 kPa) than G'' (0.84 kPa) and a decrease in value for a given frequency indicates that the copolymers have interconnected networks with water trapped either inside the tubes or in the interstitial spaces of the HNTs.

Due to their unique biocompatibility (Fig. S8 and S9, ESI†), we attempted to apply the HNTs for diabetic wound healing in Wistar rats. The rats were anaesthetized and lacerated using a surgical blade (~10 mm); this incision caused a focal disruption of the epithelial basement membrane, endothelial cell lining, and connective tissue cells (Fig. 5a).

Monitoring of diabetic wound closure in Wistar rats was performed at 1, 2, 4, 6, 8, 10, 12, 14, and 16 days. In the treated group, wound healing was significantly greater on day 10 w.r.t. the control (day 10: 55 ± 5% *vs.* 25 ± 5%, $p < 0.05$), indicating that the HNTs accelerated wound healing in diabetic rats. On day 13, the wounds of diabetic rats demonstrated enhanced recovery potential by 90 ± 5%, which was greater than those in the control group (60 ± 5%). The wounds in diabetic rats were completely healed on day 16, whereas in the control group, the wound healing rate reached 80 ± 5%, primarily from panniculus carnosus-mediated contraction. We did not observe any festering or hypertrophic scarring at the wound site during the experiments, and the appearance of fur was observed at day 16.

In the control group, disruption of blood vessels and extravasation of blood constituents caused induction of coagulation cascades, manifesting the formation of a biopolymeric plug at the wound site that primed the wound niche for repair. As the draining capacity of the vessels was largely compromised, a consortia of inflammatory cells including neutrophils and macrophages was activated, which hinders wound healing for a longer time.[61] The pro-inflammatory cytokines IL-6 and TNF-α secreted by the macrophages are the major players in the induction of acute phase response. Due to their superior biocompatibility, we sought to utilize our HNTs in an optimal local healing milieu (Fig. 5b).

For the treated group, the HNTs encouraged rapid migration and proliferation of keratinocytes at the margins of the incision in synchrony due to the 'free-edge' effect. The amphiphilicity of the HNTs favors an increased rate of reepithelialization following fibroplasia; this supports the production of ECM compounds such as hyaluronan, fibronectin, collagen, and proteoglycans,[62] which accentuates endothelial cell sprouting and stimulates neovascularisation, as observed at day 5 in the treated group. However, these nano-to-micro hierarchical patterned HNTs played a profound role in controlling wound moisture, adsorbing exudates, space-filling,[63,64] controlling oxygen tension, and wound bed restoration by forming a provisional matrix as well as painless debridement, preventing loss of water, ingress of microorganisms and specks of dirt,

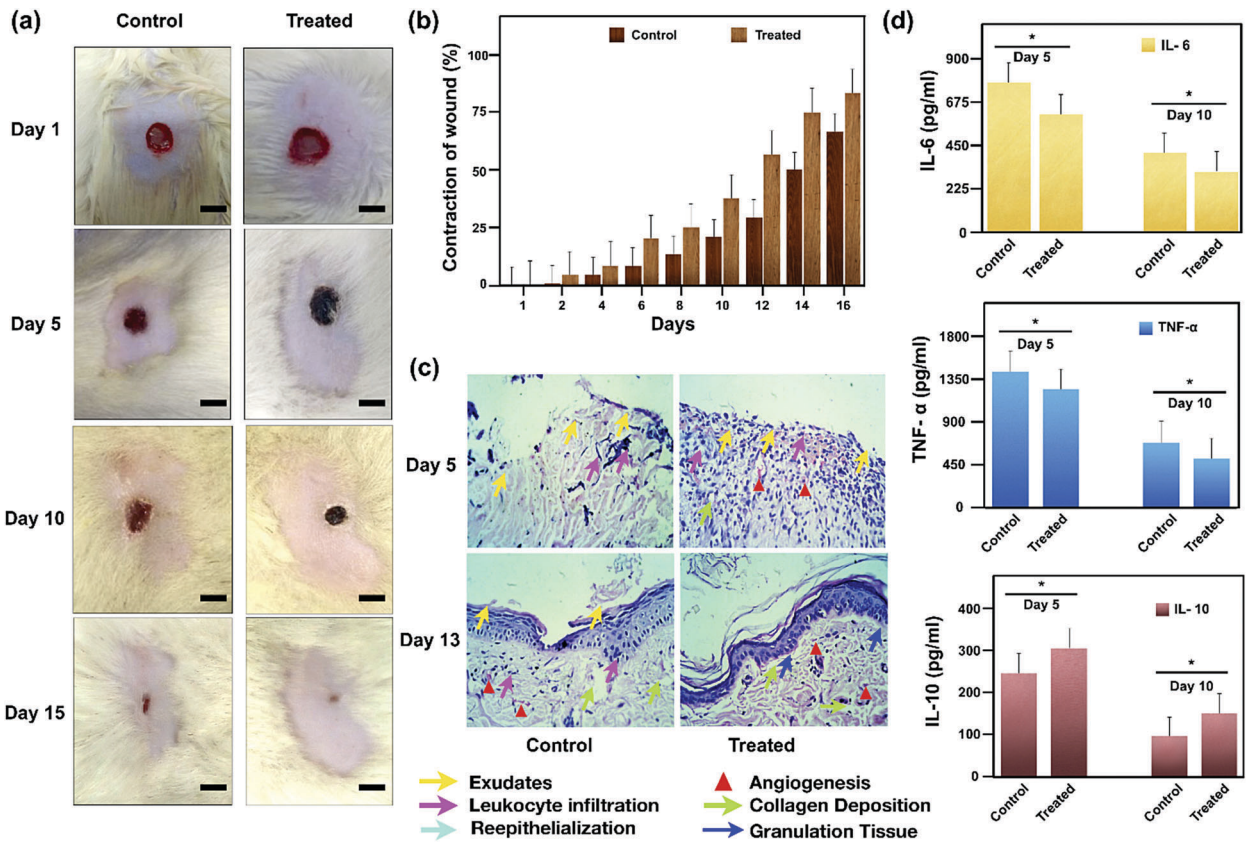

Fig. 5 *In vivo* assessment of wound healing. (a) *In vivo* study depicting control and HNT treated photograph of Wistar rat wounds at days 1, 5, 10, and 15. Control (Panel I); Treated (Panel II). Scale bar 10 mm. (b) The dermal wound contraction area at different postwounding days as a percentage with respect to the original wound size. (c) Histological assessment of diabetic wounds at days 5 and 13. Control (Panel I); Treated (Panel II) at 40×. (d) Quantification of IL-6, TNF-α and IL-10 at days 5 and 10 post-wounding. Data are represented as mean ± SEM, $n = 6$. $p < 0.05$* when the experimental groups were compared with the control group.

and overall wound dehydration. Wound healing was enhanced in the treated rats with respect to the control because reepithelialization was quicker in the moist environment, as corroborated by the significant decreases in IL-6 and TNF-α concentration at days 5 and 10 in HNT-treated diabetic rats. Collagen margins were visualized close to the incision layer by day 5 in the test group (Fig. 5c). These ultra-low-biofouling HNTs prevented non-specific protein adsorption on their surfaces, effectively alleviating foreign body response and resisting the formation of a collagenous capsule around the material. The HNTs may act as an effective "molecular sink," curbing excessive recruitment of immune cells and thereby resolving the inflammatory phase quickly,[64] as assessed by the significant increase in IL-10 concentration compared to the control group. The HNTs facilitated the formation of structured granulation tissue with high cellular density by day 5, indicating significant neovascularisation. The gradual decreases in TNF-α and IL-6 by day 10 are related to the pro-healing phenotype, which promotes tissue remodeling and regeneration.

In contrast, the control tissue displayed vascular insufficiency and limited cell recruitment to the denuded territories, delaying wound healing (Fig. 5c). We believe that an orchestrated interaction of cells with the HNTs at the wound bed synergistically improves healing.[12] Thus, the inhibition potential of IL-6 and TNF-α and a concomitant upregulation of IL-10 revealed the anti-inflammatory potential of the HNTs, whereas low IL-10 prolonged the inflammatory phase in the control group (Fig. 5c and d). By day 16, differentiation of surface cells produced a mature epidermal architecture, establishing a basement membrane and dermis consisting of multiple layers of fibrous connective tissues (Fig. 5c).

Conclusions

Motivated by a sophisticated hydrogel architecture, we have successfully fabricated hydrogel nanotubes *via* aqueous copolymerization, fulfilling a wide range of possibilities for hierarchical assembly at the nanoscale. Our results indicate that at a particular temperature, buckling of the polymer nanosheets formed tubes inspired by the art of origami with a seamless pattern. The promise of nano-confinement and non-covalent interactions between the entrapped water molecules and crystalline core encouraged the formation of a quasi-1D ice helix. Endowed with good mechanical properties and biocompatibility, an excellent wound healing outcome was realized in diabetic Wistar rats because the HNTs ameliorated early reconstruction of damaged tissue *via* a heuristic symphony of interactions with the biological milieu without relying on invasive procedures, eliminating the possibility of infection. The hope of countermanding the limitations of various biomedical applications using bioorthogonal click chemistry for multi-scale engineering of HNTs is on the horizon.

Author contributions

Monalisa Mukherjee, Rohan Bhattacharya, and Aarti Singh wrote the main manuscript text and prepared the figures. Adeeba Shakeel, Sampathkumar Jeevanandham, and Himadri B. Bohidar performed the mechanical and TGA studies. Sourav Chattopadhyay, Himadri B. Bohidar, and Sandip Chakrabarti were involved in the XRD experiments. Aarti Singh, Adeeba Shakeel, Arun Kumar Sharma, Ashish Kumar, and Satendra Kumar Rajput carried out the biological studies. Sourabh Ghosh was involved in the DSC studies. All authors have given their approval to the final version of the manuscript.

Conflicts of interest

There are no conflicts to declare.

Acknowledgements

Monalisa Mukherjee thanks the Department of Biotechnology (DBT) BT/PR21866/NNT/28/1145/2016 and Department of Science and Technology (DST), Science and Engineering Research Board (SERB) (EMR/2016/00561) for funding this project, and Amity University Uttar Pradesh (AUUP) Noida for providing research infrastructure. The group is thankful to Dakshi Kochhar for helping with the graphical abstract and Sujata Sangam for her valuable comments.

References

1 S. Iijima, *Nature*, 1991, **354**, 56.
2 B. Wong, S. Yoong, A. Jagusiak, T. Panczyk, H. Ho, W. Ang and G. Pastorin, *Adv. Drug Delivery Rev.*, 2013, **65**, 1964.
3 L. Tong, Y. Liu, B. Dolash, Y. Jung, M. Slipchenko, D. Bergstrom and J. Cheng, *Nat. Nanotechnol.*, 2011, **7**, 56.
4 X. Tang, S. Bansaruntip, N. Nakayama, E. Yenilmez, Y. Chang and Q. Wang, *Nano Lett.*, 2006, **6**, 1632.
5 J. Port and D. Murphy, *Curr. Biol.*, 2017, **27**, 1173.
6 K. Kostarelos, A. Bianco and M. Prato, *Nat. Nanotechnol.*, 2009, **4**, 627.
7 S. Hussain, Z. Ji, A. Taylor, L. DeGraff, M. George, C. Tucker, C. Chang, R. Li, J. Bonner and S. Garantziotis, *ACS Nano*, 2016, **10**, 7675.
8 J. Chen, S. Chen, X. Zhao, L. Kuznetsova, S. Wong and I. Ojima, *J. Am. Chem. Soc.*, 2008, **130**, 16778.
9 A. Nel, *Science*, 2006, **311**, 622.
10 Y. Liu, Y. Zhao, B. Sun and C. Chen, *Acc. Chem. Res.*, 2012, **46**, 702.
11 N. Joshi, J. Yan, S. Levy, S. Bhagchandani, K. Slaughter, N. Sherman, J. Amirault, Y. Wang, L. Riegel, X. He, T. Rui, M. Valic, P. Vemula, O. Miranda, O. Levy, E. Gravallese, A. Aliprantis, J. Ermann and J. Karp, *Nat. Commun.*, 2018, **9**, 1275.
12 Y. S. Zhang and A. Khademhosseini, *Science*, 2017, **356**, 6337.
13 G. Yu, X. Zhao, J. Zhou, Z. Mao, X. Huang, Z. Wang, B. Hua, Y. Liu, F. Zhang, Z. He, O. Jacobson, C. Gao, W. Wang, C. Yu, X. Zhu, F. Huang and X. Chen, *J. Am. Chem. Soc.*, 2018, **140**, 8005.
14 P. C. Nicolson and J. Vogt, *Biomaterials*, 2001, **22**, 3273.

15 S. Chawla, S. Midha, A. Sharma and S. Ghosh, *Adv. Healthcare Mater.*, 2018, **7**, 1701204.
16 N. Mitrousis, A. Fokina and M. Shoichet, *Nat. Rev. Mater.*, 2018, **3**, 441.
17 A. Neto, P. Levkin and J. Mano, *Mater. Horiz.*, 2018, **5**, 379.
18 H. Ooi, S. Hafeez, C. van Blitterswijk, L. Moroni and M. Baker, *Mater. Horiz.*, 2017, **4**, 1020.
19 E. Ruskowitz and C. DeForest, *Nat. Rev. Mater.*, 2018, **3**, 17087.
20 K. T. Huang, Y. L. Fang, P. S. Hsieh, C. C. Li, N. T. Dai and C. J. Huang, *J. Mater. Chem. B*, 2016, **4**, 4206.
21 J. F. Jhong, A. Venault, C. C. Hou, S. H. Chen, T. C. Wei, J. Zheng, J. Huang and Y. Chang, *ACS Appl. Mater. Interfaces*, 2013, **5**, 6732.
22 K. Y. Lee and D. J. Mooney, *Chem. Rev.*, 2001, **101**, 1869.
23 S. Ai, G. Lu, Q. He and J. Li, *J. Am. Chem. Soc.*, 2003, **125**, 11140–11141.
24 G. Ozaydin Ince, G. Demirel, K. Gleason and M. Demirel, *Soft Mater.*, 2010, **6**, 1635.
25 A. Gormley, R. Chandrawati, A. Christofferson, C. Loynachan, C. Jumeaux, A. Artzy-Schnirman, D. Aili, I. Yarovsky and M. Stevens, *Chem. Mater.*, 2015, **27**(16), 5820.
26 M. Steinhart, J. H. Wendorff, A. Greiner, R. B. Wehrspohn, K. Nielsch, J. Schilling, J. Choi and U. Gösele, *Science*, 2002, **296**, 1997.
27 D. Elbert and J. Hubbell, *Biomacromolecules*, 2001, **2**, 430.
28 J. Hernandez-Rojas, F. Calvo, J. Breton and J. M. G. Llorente, *J. Phys. Chem. C*, 2012, **116**, 17019.
29 A. I. Kolesnikov, J. M. Zanotti, C. K. Loong, P. Thiyagarajan, A. P. Moravsky, R. O. Loutfy and C. J. Burnham, *Phys. Rev. Lett.*, 2004, **93**(3), 035503.
30 Y. B. Zhu, F. C. Wang, J. Bai, X. C. Zeng and H. A. Wu, *ACS Nano*, 2015, **9**, 12197.
31 K. Koga, G. T. Gao, H. Tanaka and X. C. Zeng, *Nature*, 2001, **412**, 1999.
32 W. H. Zhao, L. Wang, J. Bai, L. F. Yuan, J. Yang and X. C. Zeng, *Acc. Chem. Res.*, 2014, **47**, 2505.
33 W. Zhu, Y. Zhu, L. Wang, Q. Zhu, W. H. Zhao, C. Zhu, J. Bai, J. Yang, L. F. Yuan, H. Wu and X. C. Zeng, *J. Phys. Chem. C*, 2018, **122**, 6704.
34 G. S. Longo, M. Olvera, D. Cruz and I. Szleifer, *ACS Nano*, 2013, **7**, 2693.
35 T. H. Epps and R. K. O'Reilly, *Chem. Sci.*, 2016, **7**, 1674.
36 Z. Li, M. Tang, J. Dai, T. Wang, Z. Wang, W. Bai and R. Bai, *Macromolecules*, 2017, **50**, 4292.
37 K. Matyjaszewski and J. Spanswick, *Mater. Today*, 2005, **8**, 26.
38 H. Shi, Y. Zhao, X. Dong, Y. Zhou and D. Wang, *Chem. Soc. Rev.*, 2013, **42**, 2075.
39 M. Calvaresi, M. Quintana, P. Rudolf, F. Zerbetto and M. Prato, *ChemPhysChem*, 2013, **14**, 3447.
40 K. Kobayashi, M. Koshino and K. Suenaga, *Phys. Rev. Lett.*, 2011, **106**, 18.
41 A. Goto, T. Hondoh and S. Mae, *J. Chem. Phys.*, 1990, **93**, 1412.
42 G. Algara-Siller, O. Lehtinen, F. C. Wang, R. R. Nair, U. Kaiser, H. A. Wu, A. K. Geim and I. V. Grigorieva, *Nature*, 2015, **519**, 443.
43 P. Lambin, A. Loiseau, C. Culot and L. P. Biro, *Carbon*, 2002, **40**, 1635.
44 J. S. Becker, R. D. Brown, D. R. Killelea, H. Yuan and S. J. Sibener, *Proc. Natl. Acad. Sci. U. S. A.*, 2011, **108**, 977.
45 Y. Huang, Y. Gong, F. Jiang, M. Wu, Q. Gao, W. Wei and M. Hong, *Cryst. Growth Des.*, 2007, **7**, 1385.
46 M. Brinkmann, E. Gonthier, S. Bogen, K. Tremel, S. Ludwigs, M. Hufnagel and M. Sommer, *ACS Nano*, 2012, **6**, 10319.
47 T. Babur, G. Gupta and M. Beiner, *Soft Mater.*, 2016, **12**, 8093.
48 S. Wang, S. Fabiano, S. Himmelberger, S. Puzinas, X. Crispin, A. Salleo and M. Berggren, *Proc. Natl. Acad. Sci. U. S. A.*, 2015, **112**, 10599.
49 Y. Maniwa, H. Kataura, M. Abe, A. Udaka, S. Suzuki, Y. Achiba, H. Kira, K. Matsuda, H. Kadowaki and Y. Okabe, *Chem. Phys. Lett.*, 2005, **401**, 534.
50 R. Das, S. Hamid, M. Ali, S. Ramakrishna and W. Yongzhi, *Curr. Nanosci.*, 2014, **11**, 23.
51 O. Byl, J. Liu, Y. Wang, W. Yim, J. K. Johnson and J. T. Yates, *J. Am. Chem. Soc.*, 2006, **128**, 12090.
52 T. A. Strobel, M. Somayazulu, S. V. Sinogeikin, P. Dera and R. J. Hemley, *J. Am. Chem. Soc.*, 2016, **138**, 13786.
53 A. Z. Samuel, M. Zhou, M. Ando, R. Mueller, T. Liebert, T. Heinze and H. O. Hamaguchi, *Anal. Chem.*, 2016, **88**, 4644.
54 G. H. Kim, D. Lee, A. Shanker, L. Shao, M. S. Kwon, D. Gidley, J. Kim and K. P. Pipe, *Nat. Mater.*, 2015, **14**, 295.
55 G. Song, L. Zhang, C. He, D. C. Fang, P. G. Whitten and H. Wang, *Macromolecules*, 2013, **46**, 7423.
56 S. Kutsumizu, H. Tagawa, Y. Muroga and S. Yano, *Macromolecules*, 2000, **33**, 3818.
57 K. Kruczala, B. Varghese, J. G. Bokria and S. Schlick, *Macromolecules*, 2003, **36**, 1899.
58 J. Y. Sun, X. Zhao, W. R. K. Illeperuma, O. Chaudhuri, K. H. Oh, D. J. Mooney, J. J. Vlassak and Z. Suo, *Nature*, 2012, **489**, 133.
59 D. King, T. Sun, Y. Huang, T. Kurokawa, T. Nonoyama, A. Crosby and J. Gong, *Mater. Horiz.*, 2015, **2**, 584.
60 D. Suhag, R. Bhatia, S. Das, A. Shakeel, A. Ghosh, A. Singh, O. Sinha, S. Chakrabarti and M. Mukherjee, *RSC Adv.*, 2015, **5**, 53963.
61 D. Marino, J. Luginbühl, S. Scola, M. Meuli and E. Reichmann, *Sci. Transl. Med.*, 2014, **6**, 221.
62 S. Ramasastry, *Clin. Plast. Surg.*, 2005, **32**, 195.
63 U. D. S. Sekhon and A. Sen Gupta, *ACS Biomater. Sci. Eng.*, 2018, **4**, 1176.
64 N. Lohmann, L. Schirmer, P. Atallah, E. Wandel, R. A. Ferrer, C. Werner, J. C. Simon, S. Franz and U. Freudenberg, *Sci. Transl. Med.*, 2017, **9**(386), 9044.

